Nano Research

Open Access

Research Article

Surface-reconstructed nanoporous (CoNiFe)OOH modulated by $Zn(OH)_4^{2-}$ anions: A synergistic strategy for enhanced oxygen evolution reaction electrocatalysis

Shuozhan Bai[1], Weiji Dai[1] ✉, Xin Chen[1], Fan Zhang[1], Weiguo Chen[1], Bing Wu[1], Cuijiao Zhao[1], Jing Guo[2], and Saifang Huang[1] ✉

[1] School of Materials Science and Engineering, Jiangsu University of Science and Technology, Zhenjiang 212100, China
[2] School of Resources and Materials, Northeastern University at Qinhuangdao, Qinhuangdao 066004, China

Cite this article: *Nano Research*, **2025**, *18*, 94907809. https://doi.org/10.26599/NR.2025.94907809

ABSTRACT: The sluggish kinetics of the oxygen evolution reaction (OER) severely limits the efficiency of electrochemical water splitting for sustainable hydrogen production. Developing cost-effective and efficient OER electrocatalysts based on earth-abundant elements is thus highly desirable. Herein, we report a nanoporous (CoNiFe)OOH electrocatalyst decorated with $Zn(OH)_4^{2-}$ anions, synthesized via electrochemical surface reconstruction of ZnO-decorated CoNiFe medium-entropy alloys (MEAs). The reconstructed (CoNiFe)OOH adsorbed with $Zn(OH)_4^{2-}$ anions serves as the real active phase, featuring abundant catalytic sites and enhanced OH^- accessibility. Adsorbed $Zn(OH)_4^{2-}$ anions promote OH^- transfer and facilitate electron redistribution at the active sites, particularly enhancing Co site activity, as revealed by density functional theory (DFT) calculations. As a result, the optimized CoNiFeZn@NF-EO electrode exhibits outstanding OER performance, achieving a low overpotential of 264 mV at 10 $mA \cdot cm^{-2}$, a Tafel slope of 46.6 $mV \cdot dec^{-1}$, and remarkable long-term stability in alkaline electrolyte. This work provides new insights into the synergistic effect between surface reconstruction and Zn-based species, offering a promising strategy for designing high-performance OER electrocatalysts.

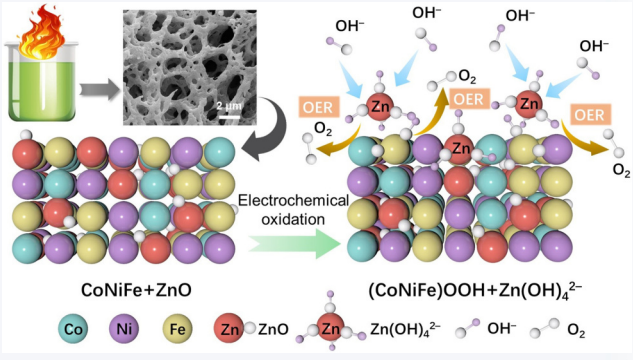

KEYWORDS: electrocatalysis, water splitting, surface reconstruction, transition metal oxy-hydroxides, medium-entropy alloys (MEAs)

1 Introduction

The oxygen evolution reaction (OER) plays a critical role in electrochemical energy conversion technologies, such as hydrogen generation via water splitting [1]. Due to the complex four-electron transfer process involved, OER typically suffers from sluggish kinetics, resulting in a high overpotential for overall water splitting [2, 3]. Considerable efforts have been devoted to developing efficient anode materials to lower this potential. Although noble metal-based oxides are currently recognized as the state-of-the-art OER catalysts, their high cost significantly limits large-scale application in hydrogen production industries [4, 5]. Recently, 3*d* transition metal-based materials have emerged as promising OER electrocatalysts, owing to their earth-abundance and superior catalytic activity [6, 7]. Notably, certain Co-, Ni-, and Fe-based oxides as well as their corresponding oxyhydroxides, have demonstrated OER performance comparable to that of precious metal oxides such as RuO_2 and IrO_2 [8, 9]. Therefore, increasing attention has been directed toward 3*d* transition metal-based electrocatalysts as potential alternatives to noble metal oxides.

Among various 3d metal oxides, ZnO is generally considered catalytically inactive for OER [10]. This is primarily due to its wide bandgap (~ 3.4 eV), which hinders electron transfer during the catalytic process [11, 12]. Moreover, the 3d orbital of Zn is fully occupied (d^{10} configuration), resulting in a stable Zn^{2+} oxidation state that lacks variable valence [10]. Consequently, Zn^{2+} sites are considered inactive for binding key OER intermediates. While Zn is

Received: April 29, 2025; **Revised:** July 11, 2025
Accepted: July 15, 2025

✉Address correspondence to Weiji Dai, daiweiji@just.edu.cn; Saifang Huang, s.huang@just.edu.cn

not traditionally viewed as a direct catalytic center, its potential influence on OER electrocatalysis has garnered growing interest.

Recent studies propose two main mechanisms by which Zn may enhance the performance of OER catalysts. First, Zn can act as an electron acceptor or donor, thereby modulating the electronic structure and valence state of adjacent active sites [13]. This electronic regulation helps optimize the adsorption energy of OER intermediates and prevent over-oxidation of catalytic centers [14]. For example, Zhou et al. demonstrated that the electron-donating Co and Zn could suppress the over-oxidation of $Ru^{n>4+}$, thereby reducing Ru leaching and enhancing the stability of Ru-based OER catalysts [15]. Second, incorporation of Zn in oxyhydroxides has been shown to activate the lattice oxygen mechanism (LOM), which bypasses the linear scaling constraints of the conventional adsorbed evolution mechanism (AEM) [16]. Huang et al. reported that Zn doping induces a shift from AEM to LOM in NiOOH, improving both the stability and activity [17]. A similar activation of LOM has been observed in MoZn-based high-entropy alloy (HEA) catalysts such as MoZnFeCoNi [18].

However, ZnO represents one type of oxide that is unstable as the OER electrocatalyst, which intends to existed as the thermodynamically stable $Zn(OH)_4^{2-}$ anions in alkaline media [19, 20]. Different from other non-catalytic oxides, such as the thermodynamically stable Cr_2O_3 which can act as a substrate for active sites [21], the introduction of ZnO in OER electrocatalysts may lead to the formation of anions adsorbed on real active materials. Therefore, the potential effects of adsorbed anions on active materials for OER electrocatalysis needs further exploration to understand the unique advantages of ZnO.

In this work, we introduce a novel nanoporous (CoNiFe)OOH electrocatalyst decorated with $Zn(OH)_4^{2-}$ anions, synthesized through a surface reconstruction strategy. Starting with ZnO-decorated hierarchical porous CoNiFe medium entropy alloys (MEAs), electrochemical oxidation generates nanoporous (CoNiFe)OOH layers decorated with surface-adsorbed $Zn(OH)_4^{2-}$ species. The presence of these anions facilitates the continuous transfer of OH^- to Co, Ni, and Fe active sties, thereby accelerating OER kinetics. Furthermore, $Zn(OH)_4^{2-}$ adsorption significantly lowers the theoretical overpotential at Co sites. The optimized CoNiFeZn@NF-EO electrode exhibits outstanding OER performance, achieving a low overpotential of 264 mV at 10 $mA{\cdot}cm^{-2}$ and a Tafel slope of 46.6 $mV{\cdot}dec^{-1}$ in 1 M KOH solution. Impressively, it retains 94.2% of its current density after 100 h of continuous operation at 1.564 V (vs. RHE), demonstrating superior durability. This study provides a comprehensive understanding of the role of $Zn(OH)_4^{2-}$ in oxyhydroxides for OER catalysis, and offers valuable insights for the design of efficient OER electrocatalysts.

2 Experimental

2.1 Chemicals

Zinc nitrate ($Zn(NO_3)_2{\cdot}6H_2O$, ≥ 98%), cobalt nitrate ($Co(NO_3)_2{\cdot}6H_2O$, ≥ 98%), nickel nitrate ($Ni(NO_3)_2{\cdot}6H_2O$, ≥ 98%), and ferric nitrate ($Fe(NO_3)_3{\cdot}9H_2O$, ≥ 98%) were bought from Shanghai Aladdin Biochemical Technology Co., Ltd. Glycine ($C_2H_5NO_2$, ≥ 98%) and potassium hydroxide (KOH, ≥ 85%) were purchased from Sinopharm Chemical Reagent Co., Ltd. All chemicals were used as received without further purification. The nickel foam (NF) with a thickness of 1 mm was purchased from Wingrise Energy Technology Co., Ltd., and used as the substrate for the electrocatalysts. After being cut into the specific shapes (working area: 1 cm × 1 cm), the NF was sequentially cleaned in 3 M HCl solution, absolute alcohol, and deionized water to remove the nickel oxide on the surface.

2.2 Synthesis of NiFe@NF, CoNiFe@NF, CoNiFeZn@NF, and $CoNiFeZn_{1.4}$@NF electrodes

The CoNiFeZn samples were synthesized directly on the NF surface using a solution combustion method (Scheme 1). Initially, 1.0 mmol each of $Co(NO_3)_2{\cdot}6H_2O$, $Ni(NO_3)_2{\cdot}6H_2O$, $Fe(NO_3)_3{\cdot}9H_2O$, $Zn(NO_3)_2{\cdot}6H_2O$, and 7.5 mmol glycine were dissolved in 4.0 mL deionized water to form a homogeneous solution. Secondly, two pretreated NF pieces were immersed in 1.0 mL of this solution placed in a beaker. The beaker was heated to 300 °C at a rate of 5 °C·min^{-1} in a furnace without further heat preservation, followed by natural cooling to room temperature. The resulting NF, decorated with CoNiFe alloys and ZnO, was used directly as the working electrode.

Preparation of the NiFe@NF, CoNiFe@NF and

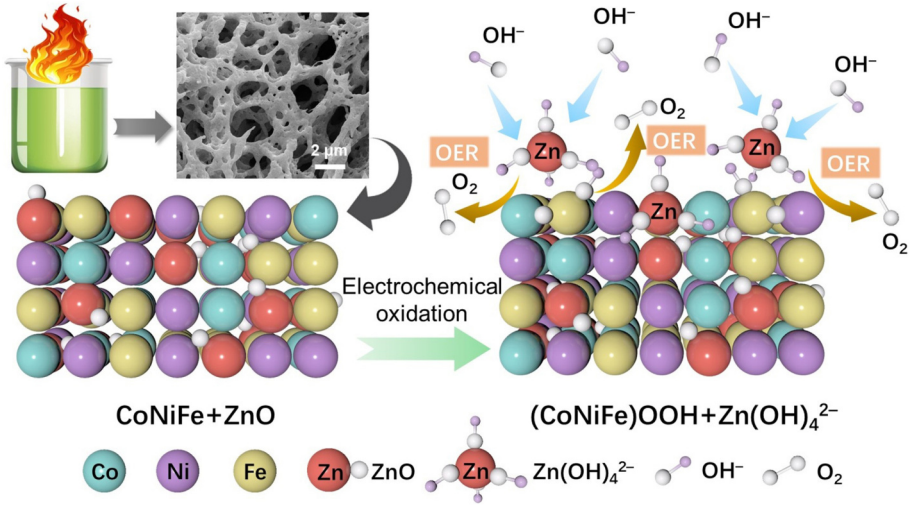

Scheme 1 Schematic illustration for the preparation of CoNiFeZn@NF electrode via a solution combustion synthesis and subsequent surface reconstruction through electrochemical oxidation.

$CoNiFeZn_{1.4}$@NF electrodes followed the same procedure as for CoNiFeZn@NF, except for variations in the glycine, $Co(NO_3)_2{\cdot}6H_2O$, and $Zn(NO_3)_2{\cdot}6H_2O$ concentrations in the precursor solution. For NiFe@NF, 4.17 mmol glycine was used without both $Co(NO_3)_2{\cdot}6H_2O$ and $Zn(NO_3)_2{\cdot}6H_2O$. For CoNiFe@NF, 5.84 mmol glycine was used without $Zn(NO_3)_2{\cdot}6H_2O$. For $CoNiFeZn_{1.4}$@NF, 8.17 mmol glycine and 1.4 mmol $Zn(NO_3)_2{\cdot}6H_2O$ were used.

2.3 Materials characterization

X-ray diffraction (XRD, D2 Phaser, Bruker AXS) using Cu Kα radiation (λ = 1.5418 Å) was conducted to examine the crystal structure over a 2θ range of 10° to 90° at a step size of 0.02°. Surface morphology and structure were examined using scanning electron microscopy (SEM, Quanta 250 FEG, Thermo Fisher Scientific Inc.) and transmission electron microscopy (TEM, Tecnai G2 F30 S-TWIN, FEI). *In-situ* Raman spectra were recorded using a HORIBA HR EVO Raman system. Surface chemical composition were analyzed via X-ray photoelectron spectroscopy (XPS, Kratos-AXIS system), with the C 1s peak at 284.8 eV used for spectral calibration [22].

2.4 Electrochemical measurements

All electrochemical measurements were carried out on a CHI 660E electrochemical workstation using a standard three-electrode setup in 1 M KOH at 25 ℃. An Ag/AgCl electrode served as the reference electrode and a Pt foil as the counter electrode. All potentials were converted to the reversible hydrogen electrode (RHE) scale using the Nernst equation: $E_{RHE} = E_{Ag/AgCl} + 0.0592 \times pH + 0.197$, where the pH value was measured using a pH meter. Cyclic voltammetry (CV) was conducted at a scan rate of 2 mV·s^{-1} within the potential range of 0–0.7 V (vs. Ag/AgCl) to determine the overpotentials for OER electrocatalysis. The electrochemical active surface area (ECSA) was evaluated via double-layer capacitance (C_{dl}), obtained from CVs at various scan rates in the non-Faradaic region. Electrochemical impedance spectroscopy (EIS) measurements were performed at 1.50 V (vs. RHE) over a frequency range of 0.01 Hz to 100 kHz with a 5 mV amplitude. In addition, *in-situ* EIS measurements were performed on both CoNiFe@NF and CoNiFeZn@NF at a voltage ranging from the open-circuit potential (OCP) to 1.60 V (vs. RHE) with 0.05 V intervals. Corrosion potentials were derived from Tafel plots measured between −1.4 and 0.4 V (vs. Ag/AgCl). Long-term OER stability was assessed through chronoamperometry at a constant current density of 50 mA·cm^{-2}.

2.5 Density functional theory (DFT) calculations

Spin-polarized DFT calculations were performed using the Vienna *ab-inito* simulation package (VASP) [23, 24]. Exchange-correlation interactions were treated with the Perdew–Burke–Ernzerhof (PBE) functional within the generalized gradient approximation (GGA) framework [25, 26]. The core-valence interactions were described using the projected augmented wave (PAW) method [27]. The energy cutoff for plane-wave basis sets was set at 400 eV. A 2 × 3 × 1 Monkhorst–Pack *k*-point mesh was employed for to Brillouin zone sampling. Structures were optimized with convergence criteria of 1.0 × 10^{-4} eV for energy and 0.05 eV·Å^{-1} for force. The initial (CoNiFe)OOH surface model consists of a metal hydroxide layer with $Zn(OH)_4^{2-}$ anions adsorbed on the outermost surface. The surface model was cleaved from the (100) facet of bulk (CoNiFe)OOH with Co, Ni, and Fe in an equimolar ratio of 1:1:1. The $Zn(OH)_4^{2-}$-(CoNiFe)OOH system comprises 105 atoms with a simulation cell measuring 12.15 Å × 8.88 Å × 22.02 Å. A vacuum slab of 15 Å along the *z*-axis was introduced to avoid interlayer interactions. Details of the Gibbs free energy calculations are provided in the Electronic Supplementary Material (ESM).

3 Results and discussion

SEM images in Fig. S1(a) in the ESM show that the prepared CoNiFeZn samples exhibit a porous morphology closely integrated with the NF substrate. Figures 1(a)–1(c) further confirm that all the CoNiFe, CoNiFeZn, and $CoNiFeZn_{1.4}$ samples detached from the NF substrate display well-defined porous frameworks. Figure S1(b) in the ESM clearly reveals the micron-scale porous skeleton of the obtained CoNiFeZn samples. Notably, there are many submicron-sized pores formed on the skeleton as shown in Fig. S1(c) in the ESM. Lastly, some nanoscale pores can also be observed on the skeleton of the prepared CoNiFeZn samples in Fig. S1(d) in the ESM, indicating the multi-scale porosity structure of the solution combustion synthesized samples. This hierarchical porous structure is beneficial for maximizing the exposure of active catalytic sites and facilitating the rapid diffusion of gaseous products during the OER process [28]. Compared to the relative smooth framework of CoNiFe, the CoNiFeZn and $CoNiFeZn_{1.4}$ samples show coarser morphologies, likely due to the incorporation of Zn.

To verify the compositions, the synthesized powders were detached from the NF substrate and analyzed by XRD. As shown in Fig. 1(d), all samples exhibit characteristic diffraction peaks at 44.3°, 51.5°, and 75.8°, corresponding to the (111), (200), and (220) planes of a face-centered cubic (FCC) alloy, respectively. The XRD pattern in Fig. S2 in th eESM further shows the diffraction peaks of the FCC alloy shifted to lower 2θ values compared to metallic Ni (PDF card No. 04-0850), whose 2θ for (111) and (200) planes are 44.5° and 51.8°, respectively. This can ascribe to the alloying of larger heteroatoms such as Fe and Co into the lattice of Ni, thus expanding its lattice. As a result, the obtained FCC alloy is identified to be the face-centered cubic CoNiFe alloy [29]. Additional peaks at 31.8°, 34.5°, 36.3°, 47.6°, 56.7°, 63.0°, and 68.1° are observed in the diffraction patterns of CoNiFeZn and $CoNiFeZn_{1.4}$ samples, corresponding to the (100), (002), (101), (102), (110), (103), and (112) planes of ZnO (PDF card No. 75-0576), respectively. These results confirmed the formation of ZnO, which is likely responsible for the observed coarsening of the framework in the CoNiFeZn and $CoNiFeZn_{1.4}$ samples. Elemental mapping via Energy-dispersive X-ray spectroscopy (EDS) (Fig. 1(e)) reveals a uniform distribution of Ni, Fe, Co, Zn, and O across the porous frameworks, demonstrating the successful and homogeneous integration of ZnO within the matrix of CoNiFe MEAs.

The OER performance of NiFe@NF, CoNiFe@NF, CoNiFeZn@NF, and $CoNiFeZn_{1.4}$@NF electrodes were evaluated in 1 M KOH solution at 25 ℃. To assess the potentials for OER electrocatalysis, CV curves obtained at a scan rate of 2 mV·s^{-1} (without *iR*-compensation) are shown in Fig. 2(a). As illustrated in Fig. 2(b), the CoNiFeZn@NF electrode exhibits the lowest overpotential of 272 mV at 10 mA·cm^{-2} (η_{10}), outperforming NiFe@NF (281 mV), CoNiFe@NF (279 mV), and $CoNiFeZn_{1.4}$@NF (277 mV). At a higher current density of 100 mA·cm^{-2} (η_{100}), CoNiFeZn@NF also shows superior performance with an overpotential of 415 mV compared to

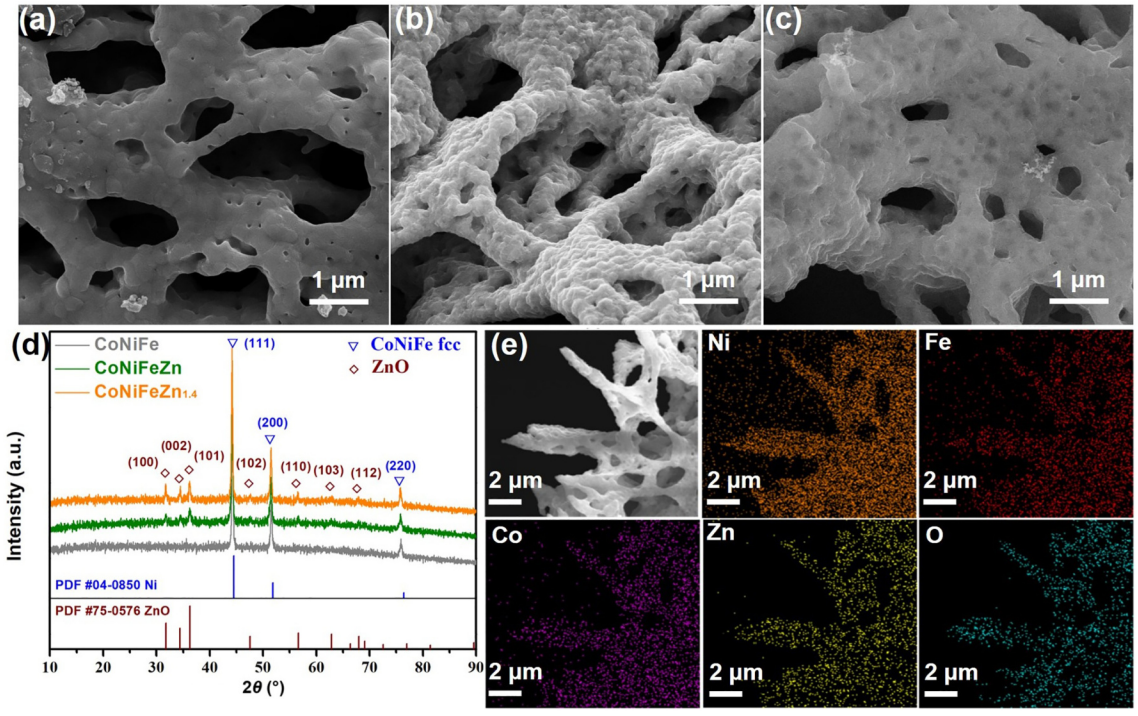

Figure 1 (a)–(c) SEM images of CoNiFe, CoNiFeZn, and CoNiFeZn$_{1.4}$ samples, respectively. (d) XRD patterns of the corresponding powders detached from the NF substrate. (e) EDS elemental mapping of CoNiFeZn, confirming uniform distribution of Co, Ni, Fe, Zn, and O.

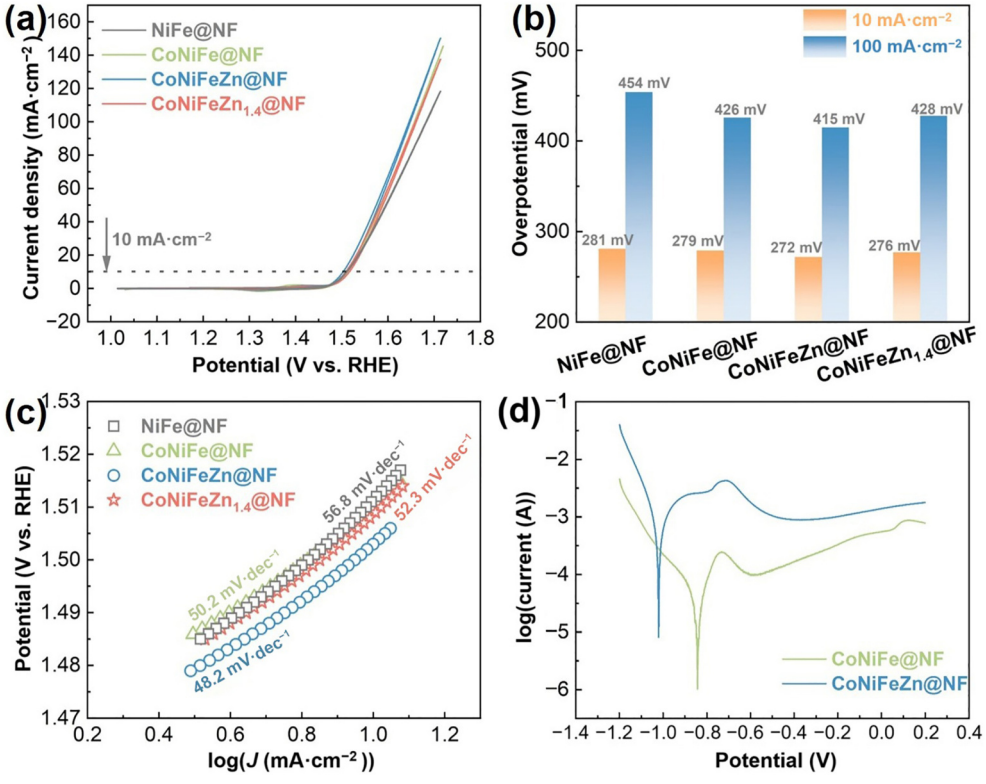

Figure 2 (a) CV curves of NiFe@NF, CoNiFe@NF, CoNiFeZn@NF, and CoNiFeZn$_{1.4}$@NF electrodes at 2 mV·s^{-1} without *iR*-compensation. (b) Overpotentials at 10 and 100 mA·cm^{-2} for the three electrodes. (c) Tafel slopes comparing reaction kinetics. (d) Tafel plots comparing the corrosion potentials of different electrodes.

NiFe@NF (454 mV), CoNiFe@NF (426 mV), and CoNiFeZn$_{1.4}$@NF (428 mV). Tafel slope analysis (Fig. 2(c)) further support these findings. The CoNiFeZn@NF electrode exhibits the lowest Tafel slope (48.2 mV·dec^{-1}), indicating its enhanced OER kinetics compared to NiFe@NF (56.8 mV·dec^{-1}), CoNiFe@NF (50.2 mV·dec^{-1}), and CoNiFeZn$_{1.4}$@NF (52.3 mV·dec^{-1}). Additionally, CoNiFeZn@NF shows a significantly corrosion potential (−1.02 V vs. Ag/AgCl) than CoNiFe@NF (−0.84 V vs. Ag/AgCl), indicating a more reactive surface under alkaline conditions (Fig. 2(d)). This increased reactivity facilitates surface

reconstruction during OER, thereby influencing electrocatalytic performance.

To explore the impact of surface reconstruction, 3-h chronoamperometry tests were performed at potentials corresponding to about 20 mA·cm^{-2} for each electrodes. As shown in Fig. 3(a), the OER current density of NiFe@NF and CoNiFe@NF decrease by 30.0% and 6.5% respectively, indicating obvious performance degradation. In contrast, CoNiFeZn@NF and CoNiFeZn$_{1.4}$@NF exhibited increases of 18.5% and 22.2%, respectively, highlighting the beneficial role of ZnO incorporation in enhancing OER performance upon electrochemical oxidation. This improvement is attributed to the formation of $Zn(OH)_4^{2-}$ anions and nanoporous (CoNiFe)OOH because of surface reconstruction, which will be discussed in more detail below.

Subsequent CV scans were performed on the reconstructed electrodes to evaluate the enhanced OER activity due to the electrochemical oxidation (Fig. 3(b)). As shown in Fig. 3(c), the CoNiFe@NF after electrochemical oxidation (CoNiFe@NF-EO) exhibits same η_{10} (279 mV) and a slightly higher η_{100} (427 mV) compared to its pre-reconstruction state. In contrast, both CoNiFeZn@NF-EO and CoNiFeZn$_{1.4}$@NF-EO exhibit significantly reduced overpotentials, consistent with the chronoamperometry results in Fig. 3(a). Notably, CoNiFeZn@NF-EO demonstrates the best performance for OER electrocatalysis, with η_{10} = 264 mV and η_{100} = 409 mV. Figure 3(d) shows that the CoNiFeZn@NF-EO and CoNiFeZn$_{1.4}$@NF-EO electrodes also achieve improved Tafel slopes (46.6 and 47.8 mV·dec^{-1}, respectively), superior to NiFe@NF-EO (59.4 mV·dec^{-1}) and CoNiFe@NF-EO (49.6 mV·dec^{-1}), suggesting more favorable kinetics. The enhanced OER performance of CoNiFeZn@NF-EO is competitive with electrocatalysts documented in literatures, such as single-atom Ni catalysts (η_{10} = 279 mV) [30], and others recently reported electrocatalysts as shown in Table S1 in the ESM.

To further understand the enhanced OER performance of CoNiFeZn@NF-EO and CoNiFeZn$_{1.4}$@NF-EO, the ECSA of the reconstructed electrodes was calculated using the formula: ECSA = C_{dl}/C_s, where C_s is the specific capacitance of a smooth surface in alkaline media (0.04 mF·cm^{-2}) [31]. The C_{dl} values were extracted from CV curves measured at various scan rates ranging from 10 to 50 mV·s^{-1}, as shown in Fig. S3 in the ESM. The derived C_{dl} values are presented in Fig. 3(e), and the calculated ECSA values for NiFe@NF-EO, CoNiFe@NF-EO, CoNiFeZn@NF-EO, and CoNiFeZn$_{1.4}$@NF-EO with a geometric electrode area of 1 cm^2 are 217.5, 487.5, 665, and 577.5 cm^2, respectively. These C_{dl} values represent a clear increase in ECSA compared to the initial states of the electrodes prior to the electrochemical oxidation as shown in Fig. S4 in the ESM. The much larger ECSA of the CoNiFeZn@NF-EO indicates a higher density of exposed active sites, thereby

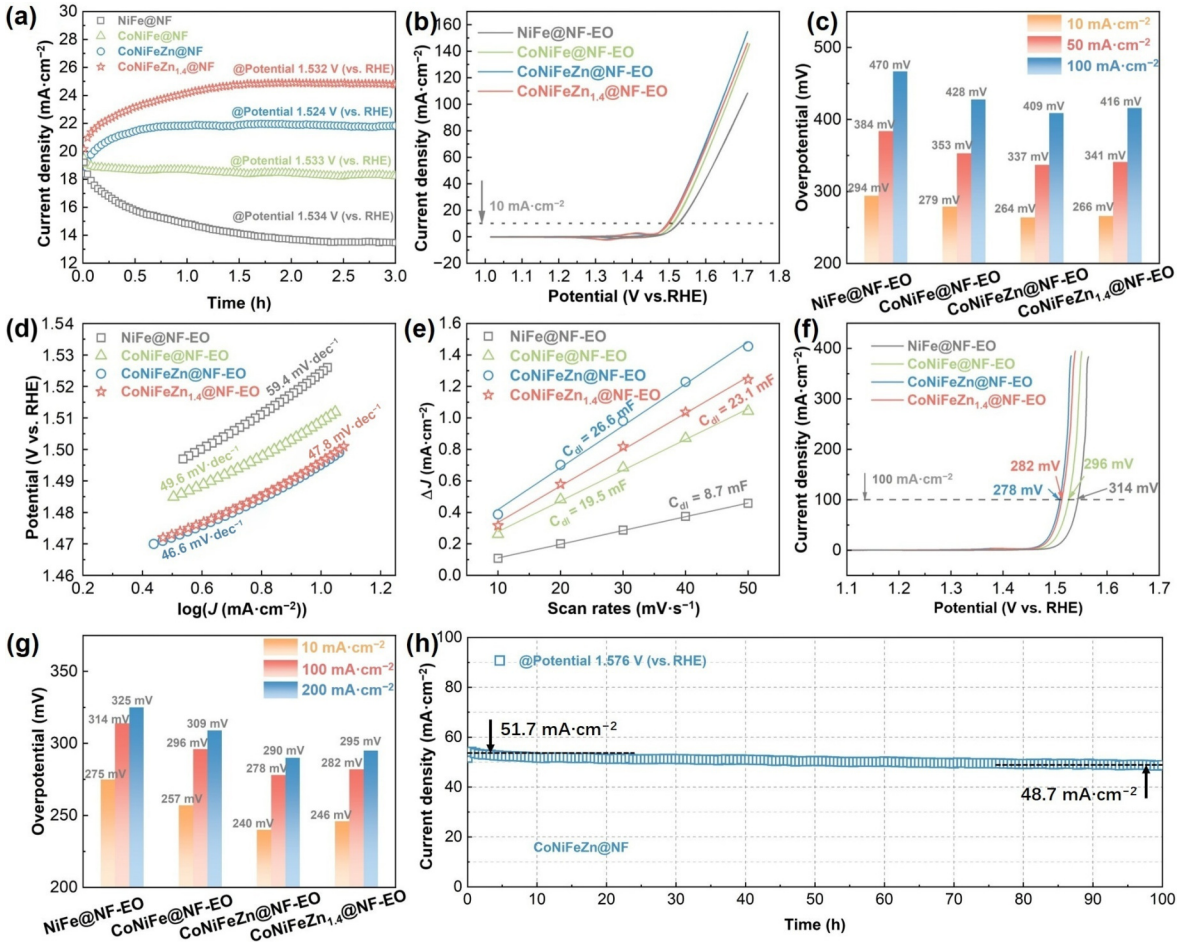

Figure 3 (a) *i*–*t* curves of NiFe@NF, CoNiFe@NF, CoNiFeZn@NF, and CoNiFeZn$_{1.4}$@NF for surface reconstruction. (b) CV curves of the reconstructed electrodes at 2 mV·s^{-1} (without *iR*-compensation). (c) Overpotentials at 10, 50 and 100 mA·cm^{-2} for the reconstructed samples. (d) Tafel slopes of the reconstructed electrodes. (e) Capacitive current density (1/2 Δ*J*) vs. scan rate at 1.11 V (vs. RHE) for estimating ECSA. (f) CV curves of the reconstructed electrodes at 2 mV·s^{-1} (with 80% *iR*-compensation). (g) *iR*-compensated overpotentials for the reconstructed electrodes. (h) *i*–*t* curve of the CoNiFeZn@NF-EO sample at 1.576 V (vs. RHE) over 100 h.

contributing to its enhanced OER electrocatalytic performance.

EIS results (Fig. S5 in the ESM) show that the charge transfer resistance (R_{ct}) values for CoNiFeZn@NF and $CoNiFeZn_{1.4}$@NF are 0.84 and 0.79 Ω, respectively. Both are lower than that of CoNiFe@NF (1.11 Ω). Additionally, the *in-situ* EIS in Fig. S6(a) in the EMS shows a decrease of the phase angle within the mid-frequency region, which corresponding to the electrochemical reconstruction of the CoNiFe@NF electrode [32]. In Fig. S6(b) in the ESM, the decrease of the phase angle for the CoNiFeZn@NF electrode is faster compared to CoNiFe@NF electrode, indicating that the introduction of ZnO facilitates the reconstruction of the electrode, which is consistent with the corrosion potentials shown in Fig. 2(d). More importantly, a sharp decline of the phase angle in the low-frequency region occurs at approximately 1.40 V (vs. RHE) for the CoNiFeZn@NF electrode, corresponding to the lower onset of the OER [33]. However, the decline is observed at about 1.45 V (vs. RHE) for the CoNiFe@NF electrode. These findings imply that the surface reconstruction, involving the formation of $Zn(OH)_4^{2-}$ species, enhance the charge transfer capabilities of the nanoporous (CoNiFe)OOH, thereby facilitating OER electrocatalysis.

The CV curves with 80% *iR*-compensation for the reconstructed electrodes are presented in Fig. 3(f). As shown in Fig. 3(g), the η_{10} and η_{100} of CoNiFeZn@NF-EO (240 and 278 mV) and $CoNiFeZn_{1.4}$@NF-EO (246 and 282 mV) are also lower than those of NiFe@NF-EO (275 and 314 mV) and CoNiFe@NF-EO (257 and 296 mV), confirming the beneficial effect of ZnO incorporation into the CoNiFe MEAs on OER activity. To assess the intrinsic activity of the derived electrocatalysts, the OER current densities were normalized by the ECSA values. As shown in Fig. S7 in the ESM, both CoNiFeZn@NF-EO and $CoNiFeZn_{1.4}$@NF-EO exhibit improved OER activity compared to NiFe@NF-EO and CoNiFe@NF-EO. This confirms that the surface-reconstructed nanoporous (CoNiFe)OOH structures decorated with $Zn(OH)_4^{2-}$ species are intrinsically more active for OER electrocatalysis. The corrosion potential of CoNiFe@NF remained nearly unchanged after 3 h of electrochemical oxidation (Fig. S8 in the ESM). In contrast, the CoNiFeZn@NF-EO exhibited a positive shift in corrosion potential from –1.02 to –0.91 V (vs. Ag/AgCl) (Fig. S9 in the ESM), indicating structural evolution during the electrochemical oxidation and an improvement in corrosion resistance.

To further evaluate the long-term durability, OER stability testing was performed on the CoNiFeZn@NF-EO electrode via chronoamperometry method. As shown by the *i*–*t* curve in Fig. 3(h), the electrode retained 94.2% of its initial current density at 1.576 V (vs. RHE) after 100 h, demonstrating superior durability and robustness for OER electrocatalysis under operational conditions. The structure and composition analysis were conducted after the 100-h OER test as displayed in Fig. S10 in the ESM. The SEM images in Figs. S10(a) and S10(b) in the ESM display the porous structure still maintained within the 100-h OER test, indicating the microstructure is stable during the electrocatalysis process. However, the EDS results shown in Figs. S10(c) and S10(d) in the ESM demonstrate that the contents of Zn obviously decreased from 10.8 at.% to 1.21 at.% after the 100-h OER test, which corresponding to the transformation of ZnO to $Zn(OH)_4^{2-}$ anions. This revealed that only parts of $Zn(OH)_4^{2-}$ anions were adsorbed on the derived (CoNiFe)OOH, and still taken positive effects for OER electrocatalysis. In addition, no significant decrease of the contents of active sites, such as the Fe, Co, and Ni sites was observed, confirming the stability in composition. Thanks to the stable porous structure and maintained active sites, the prepared electrocatalysts exhibit remarkable long-term stability for OER in alkaline electrolyte. Moreover, the η_{10} of CoNiFeZn@NF-EO further decreased to 258 mV after the 100-h test (Fig. S11 in the ESM), which can attribute to the more exposed active sites of nanoporous (CoNiFe)OOH during the oxidation process.

To elucidate the mechanism underlying the enhanced OER activity of electrochemical oxidation, detailed microstructural characterization was performed on the CoNiFeZn@NF-EO. SEM images of CoNiFeZn@NF-EO (Figs. 4(a) and 4(b)) reveal a distinct coral-like morphology, markedly different from the initial structure of the electrode. The surface reconstruction-induced coral-like architecture is expected to increase the number of exposed catalytic sites, thereby enhancing OER performance. Further insights were obtained via TEM analysis (Figs. 4(c) and 4(d)), which revealed the presence of abundant nanoporous structures surrounding the coral-like features. EDS was performed on both the coral-like domains (area 1) and the nanoporous regions (area 2), as marked in Fig. S12 in the ESM. The Zn content was measured to be 2.46 at.% in area 1 (Fig. S13 in the ESM) and 8.52 at.% in area 2 (Fig. S14 in the ESM). This provides strong evidence that Zn species formed during electrochemical oxidation are primarily adsorbed onto the nanoporous structures.

Selected area electron diffraction (SAED) was conducted on the nanoporous region (Fig. 4(d)), and the resulting diffraction rings (Fig. 4(e)) were indexed to the (100), (101), (102), and (110) planes of (FeNi)OOH (PDF card No. 14-0556), a known active phase derived from the CoNiFe MEAs for OER catalysis [34]. The high-resolution TEM image in Fig. 4(f) displays clear lattice fringes with an interplanar spacing of 0.217 nm, slightly shorter than the (111) plane of (FeNi)OOH. This can ascribe to the incorporation of Co^{3+} into the lattice of (FeNi)OOH. This is reasonable since cobalt in CoNiFe MEAs can also be oxidized during OER process, leading to the formation of (CoNiFe)OOH as the reconstructed active phase.

Additionally, the SAED pattern exhibits diffraction rings corresponding to the (411) and (211) planes of $Zn(OH)_2$ (PDF card No. 38-0356), indicating the presence of the derived Zn species because of electrochemical oxidation. It is noteworthy that under alkaline conditions, Zn^{2+} predominantly exists in the form of $Zn(OH)_4^{2-}$ [19, 20]. Hence, during the OER process in alkaline media, the introduction of ZnO into CoNiFe MEAs results in the formation of nanoporous (CoNiFe)OOH decorated with $Zn(OH)_4^{2-}$ anions. This synergistic combination contributed significantly to the observed enhancement in OER performance. Furthermore, elemental mapping (Fig. 4(g)) confirms the uniform distribution of Co, Ni, Fe, Zn and O throughout the catalyst particles, indicating homogeneous structural and compositional transformation upon reconstruction.

The chemical composition and elemental valence state of CoNiFeZn@NF before and after electrochemical oxidation were analyzed using X-ray photoelectron spectroscopy (XPS). As shown in Figs. S15(a) and S15(b) in the ESM, the XPS survey spectra confirm the presence of Co, Ni, Fe, Zn, and O in CoNiFeZn@NF and CoNiFeZn@NF-EO. The high-resolution Co 2p spectra (Fig. 5(a)) for the initial CoNiFeZn@NF exhibit two distinct peaks at 781 and 779.5 eV, corresponding to Co^{2+} $2p_{3/2}$ and Co^{3+} $2p_{3/2}$, respectively, indicating an oxidized state of cobalt on the electrode surface [35, 36]. In the Ni 2p spectra (Fig. 5(b)), deconvoluted peaks at 853.9 and 855.7 eV are attributed to Ni^{2+} $2p_{3/2}$ and Ni^{3+} $2p_{3/2}$, respectively, associated with Ni–O bonding [37, 38]. A peak at

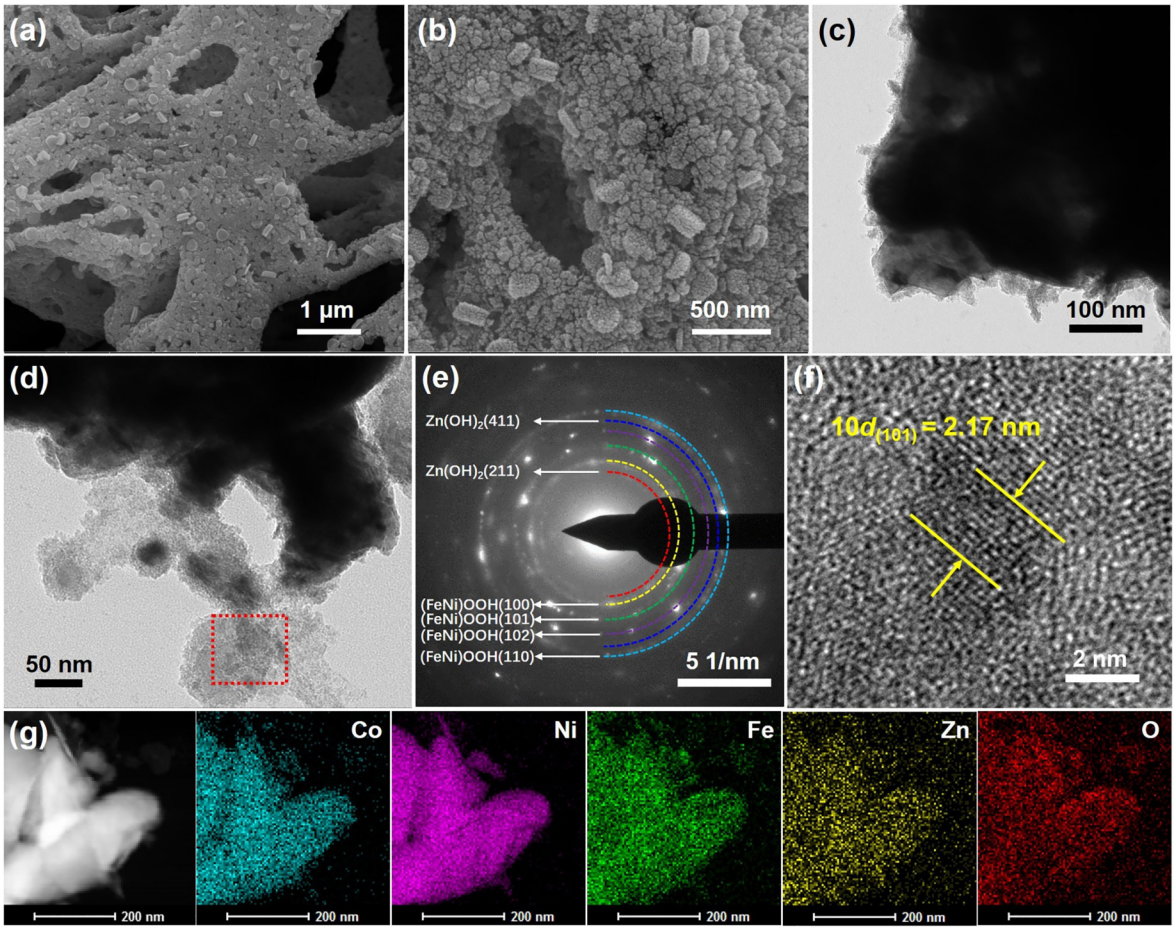

Figure 4 Post-oxidation microstructure of CoNiFeZn@NF: (a) and (b) SEM images; (c) and (d) TEM images; (e) SAED pattern from the region marked in (d); (f) high-resolution TEM image; (g) elemental mapping.

852.1 eV, corresponding to metallic Ni, is also observed and is ascribe to the formation of CoNiFe MEAs in CoNiFeZn@NF [39]. The Fe 2p spectra (Fig. 5(c)) show two primary peaks at 710.6 and 713.1 eV, corresponding to Fe^{2+} $2p_{3/2}$ and Fe^{3+} $2p_{3/2}$, respectively, indicative of Fe–O bonding [40, 41]. Notably, no peaks associated with metallic Co^0 and Fe^0 were detected, likely due to their lower content compared to the oxidized species. After the 3-h electrochemical oxidation, the XPS spectra reveal a remarkable increase in the M^{3+}/M^{2+} ratio for Co, Ni, and Fe (Table S2 in the ESM), corroborating the formation of nanoporous (CoNiFe)OOH as a result of the electrochemical oxidation [42, 43].

The Zn 2p spectra (Fig. 5(d)) display two prominent peaks at 1044.4 eV (Zn $2p_{1/2}$) and 1021.3 eV (Zn $2p_{3/2}$) for the initial CoNiFeZn@NF sample, corresponding to the Zn–O bonding in ZnO [44]. After oxidation, the Zn $2p_{1/2}$ peak exhibits a negative shift of about 0.2 eV, which is attributed to increased electron density associated with the transformation of ZnO to $Zn(OH)_4^{2-}$ anions [45]. The O 1s spectra (Fig. 5(e)) for the initial CoNiFeZn@NF show peaks at 529.5, 530.2, 530.9, and 532.0 eV, which are assigned to M–O bonds, oxygen vacancies (O_v), M–OH bonds, and adsorbed H_2O, respectively [46, 47]. Upon electrochemical oxidation, the relative content of M–OH species increased significantly from 26.5% to 46.4%, reflecting the generation of abundant oxyhydroxides and hydroxide species on the surface. These XPS findings confirm the formation of (CoNiFe)OOH and $Zn(OH)_4^{2-}$ species, in excellent agreement with the SAED results and other structural characterizations, further supporting the role of surface reconstruction in enhancing OER performance.

To further demonstrate the phase evolution of electrocatalyst, *in-situ* Raman spectroscopy was conducted on the CoNiFeZn@NF electrode under applied potentials ranging from 1.21 to 1.61 V (vs. RHE) with 0.04 V intervals. As shown in Fig. 5(f), the spectrum acquired at OCP display three characteristic peaks at 473, 610, and 690 cm^{-1}, which are attributed to Ni–O, Fe–O, and Co–O vibrations in metal oxides, respectively [17, 48]. Meanwhile, a peak at 418 cm^{-1} corresponds to the Zn–O vibration [49]. Upon increasing the applied voltage, new peaks emerge at 552.0 and 652.4 cm^{-1}, indicative of M–O vibrations in M–OOH (M = Co, Ni, Fe), confirming the formation of oxyhydroxides during oxidation [50]. Notably, a Raman peak at 471 cm^{-1} appears, associated with Zn–O vibrations that likely originate from adsorbed $Zn(OH)_4^{2-}$ anions [51]. The simultaneous presence of oxyhydroxides and Zn–OH vibrations confirms that the active material underwent significant structural transformation due to electrochemical oxidation. Thus, the enhanced OER activity of CoNiFeZn@NF following oxidation can be attributed to the formation of nanoporous (CoNiFe)OOH coupled with the adsorbed $Zn(OH)_4^{2-}$ species.

To elucidate the influence of $Zn(OH)_4^{2-}$ adsorption on the OER activity of (CoNiFe)OOH, density functional theory (DFT) calculations were performed. The (100) surface of (CoNiFe)OOH was selected to investigate the atomic-scale OER mechanism in alkaline conditions in the presence of $Zn(OH)_4^{2-}$, as illustrated in

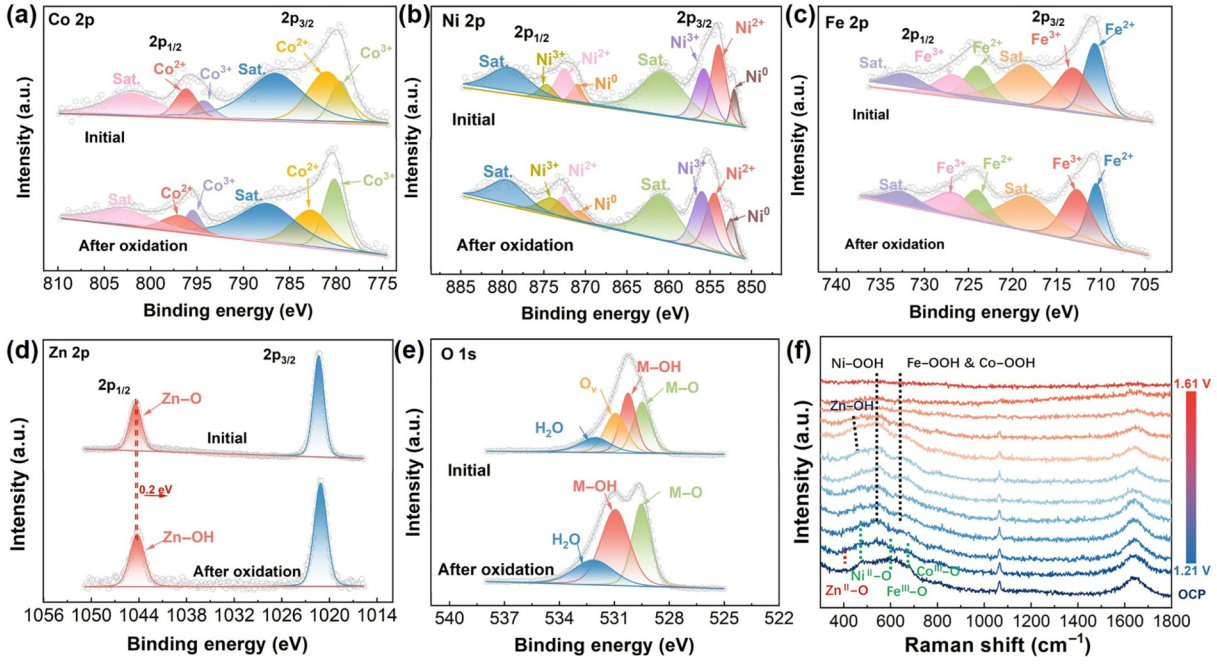

Figure 5 High-resolution XPS spectra of CoNiFeZn@NF and CoNiFeZn@NF-EO: (a) Co 2p, (b) Ni 2p, (c) Fe 2p, (d) Zn 2p, and (e) O 1s. (f) *In-situ* Raman spectra of CoNiFeZn@NF recorded from 1.21 to 1.61 V (vs. RHE) with 0.04 V intervals.

Fig. 6(a). For the adsorbed $Zn(OH)_4^{2-}$ anions, the deprotonation of *OH to *O is identified as the potential-determining step, with a high free energy barrier of 2.48 eV (Fig. 6(b)). The large barrier suggests that the Zn site may not be directly active for OER electrocatalysis, which aligns with previous findings [10]. However, the Zn site exhibits a thermodynamically favorable ability to adsorb OH^- form the electrolyte due to its high OH^- adsorption energy. Consequently, the OH^- groups adsorbed on $Zn(OH)_4^{2-}$ can transfer to Co, Ni, and Fe sites in (CoNiFe)OOH during the OER process particularly in the *O to *OOH transition step, demonstrating a synergistic catalytic effect among multiple metal centers [52].

Among these, the Co site exhibits the most favorable OER activity with a theoretical potential of 1.75 V. To further understand the origin of this activity, the projected density of states (PDOS) for the 3d orbitals of Co, Ni, Fe, and Zn were calculated for (CoNiFe)OOH (100) with $Zn(OH)_4^{2-}$ adsorption. As shown in Fig. 6(c), the d-band centers for Co, Ni, Fe, and Zn are located at −1.325, −1.526, −1.643, and −3.974 eV, respectively. Since a lower d-band center is correlated with weaker binding strength of OER intermediates [53, 54], Co exhibits the most favorable binding and, thus, the highest catalytic activity. Furthermore, charge density distribution analysis (Fig. S16 in the ESM) reveals that $Zn(OH)_4^{2-}$ adsorption can lead to electron depletion at the Co, Ni, and Fe sites, which enhances electron transfer during OER [55]. Collectively, these results suggest that $Zn(OH)_4^{2-}$ adsorption on (CoNiFe)OOH plays a vital role in promoting OER electrocatalysis by modulating surface electron density and enabling synergistic catalysis.

4 Conclusions

In summary, we developed a highly efficient OER electrocatalyst, CoNiFeZn@NF-EO, through a facile solution combustion synthesis followed by surface reconstruction. The incorporation of ZnO and subsequent electrochemical oxidation lead to the formation of a nanoporous (CoNiFe)OOH structure with adsorbed $Zn(OH)_4^{2-}$ anions. This reconstructed architecture exhibits remarkable OER performance, delivering a low overpotential of 264 mV at 10 mA·cm^{-2} (without *iR*-compensation), a small Tafel slope of 46.6 mV·dec^{-1}, and outstanding long-term stability with 94.2% current retention after 100 h at 1.576 V (vs. RHE). Structural and spectroscopic analyses confirm the formation of a nanoporous (CoNiFe)OOH and the uniform distribution of $Zn(OH)_4^{2-}$ across the catalyst surface. DFT calculations reveal that $Zn(OH)_4^{2-}$ not only enhances OH^- adsorption but also promotes electron transfer and synergistic activation at adjacent Co, Ni, and Fe sites, particularly boosting the activity at Co sites with a theoretical potential of 1.75 V. These findings provide a comprehensive understanding of the catalytic role of $Zn(OH)_4^{2-}$ and offer a promising strategy for designing cost-effective and robust OER electrocatalysts based on transition metal oxyhydroxides.

Electronic Supplementary Material: Supplementary material (details of the Gibbs free energy calculations, OER performance comparison table, XPS/SEM/XRD/TEM results, electrochemical measurements, and charge density diagrams results) is available in the online version of this article at https://doi.org/10.26599/NR.2025.94907809.

Data availability

All data needed to support the conclusions in the paper are presented in the manuscript and the Electronic Supplementary Material. Additional data related to this paper may be requested from the corresponding author upon request.

Acknowledgements

This work was financially supported by the National Natural Science Foundation of China (Nos. 52202093 and 52304325), the Natural Science Research of Jiangsu Higher Education Institutions of China (No. 22KJB430021), and Jiangsu Provincial Double-

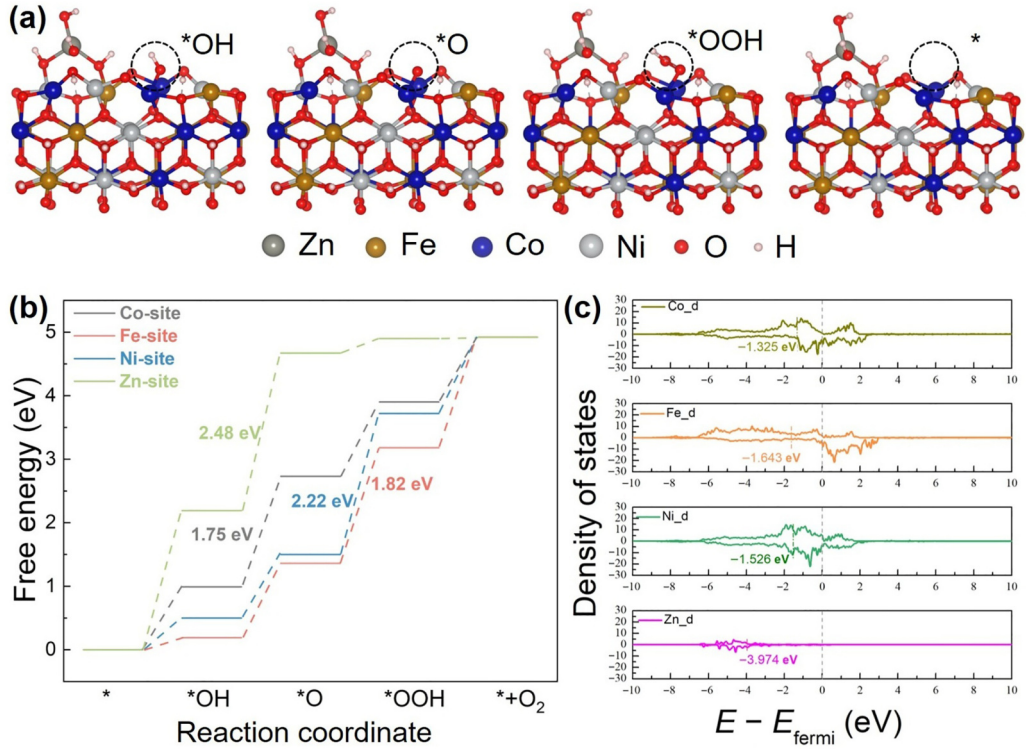

Figure 6 (a) Side view of configuration for the (CoNiFe)OOH (100) surface with $Zn(OH)_4^{2-}$ adsorption. (b) Gibbs free energy diagram for OER on (CoNiFe)OOH (100) with $Zn(OH)_4^{2-}$ adsorption under alkaline conditions. (c) Projected density of states (PDOS) for the 3d orbital of Co, Fe, Ni, and Zn on (CoNiFe)OOH (100) with $Zn(OH)_4^{2-}$ adsorption.

Innovation Doctor Program (No. JSSCBS20221258).

Declaration of competing interest

The authors declare no competing financial interest.

Author contribution statement

S. Z. B.: Data curation, investigation, writing original draft. W. J. D.: Conceptualization, funding acquisition, supervision, writing original draft. X. C.: Data curation, validation. F. Z.: Software, validation. W. G. C.: Investigation. B. W.: Resources. C. J. Z.: Funding acquisition, supervision. J. G.: Funding acquisition. S. F. H.: Funding acquisition, project administration, writing – review & editing.

Use of AI statement

None.

References

[1] Li, H. J. W.; Lin, Y.; Duan, J. Y.; Wen, Q. L.; Liu, Y. W.; Zhai, T. Y. Stability of electrocatalytic OER: From principle to application. *Chem. Soc. Rev.* **2024**, *53*, 10709–10740.

[2] He, C. S.; Yang, L. L.; Wang, J.; Wang, T. T.; Ju, J.; Lu, Y. Z.; Chen, W. Research progress on electronic and active site engineering of cobalt-based electrocatalysts for oxygen evolution reaction. *Carbon Energy* **2024**, *6*, e573.

[3] Shi, Q. R.; Zhu, C. Z.; Du, D.; Lin, Y. H. Robust noble metal-based electrocatalysts for oxygen evolution reaction. *Chem. Soc. Rev.* **2019**, *48*, 3181–3192.

[4] Nan, J.; Ye, B. R.; He, X.; Li, C.; Zhang, W. L.; Liu, Q.; Li, L. M.; Chu, W.; Sun, X. P.; Zhang, Y. Q. Enhancing alkaline water oxidation with NiFe alloy-encapsulated nitrogen-doped vertical graphene array. *Nano Res.* **2024**, *17*, 4790–4796.

[5] Wu, L.; Shen, X. P.; Ji, Z. Y.; Yuan, J. R.; Yang, S. K.; Zhu, G. X.; Chen, L. Z.; Kong, L. R.; Zhou, H. B. Facile synthesis of medium-entropy metal sulfides as high-efficiency electrocatalysts toward oxygen evolution reaction. *Adv. Funct. Mater.* **2023**, *33*, 2208170.

[6] Zhang, Y. Y.; Wu, J.; Guo, B. R.; Huo, H. H.; Niu, S. Q.; Li, S. W.; Xu, P. Recent advances of transition-metal metaphosphates for efficient electrocatalytic water splitting. *Carbon Energy* **2023**, *5*, e375.

[7] Zhang, X. Y.; Feng, C.; Dong, B.; Liu, C. G.; Chai, Y. M. High-voltage-enabled stable cobalt species deposition on MnO_2 for water oxidation in acid. *Adv. Mater.* **2023**, *35*, 2207066.

[8] Liu, X.; Meng, J. S.; Zhu, J. X.; Huang, M.; Wen, B.; Guo, R. T.; Mai, L. Comprehensive understandings into complete reconstruction of precatalysts: Synthesis, applications, and characterizations. *Adv. Mater.* **2021**, *33*, 2007344.

[9] Zhang, X.; Yi, H.; Jin, M. T.; Lian, Q.; Huang, Y.; Ai, Z.; Huang, R. Q.; Zuo, Z. T.; Tang, C. M.; Amini, A. et al. *In situ* reconstructed Zn doped $Fe_xNi_{(1-x)}OOH$ catalyst for efficient and ultrastable oxygen evolution reaction at high current densities. *Small* **2022**, *18*, 2203710.

[10] Zhou, Y.; Sun, S. N.; Xi, S. B.; Duan, Y.; Sritharan, T.; Du, Y. H.; Xu, Z. J. Superexchange effects on oxygen reduction activity of edge-sharing $[Co_xMn_{1-x}O_6]$ octahedra in spinel oxide. *Adv. Mater.* **2018**, *30*, 1705407.

[11] Ali, S. A.; Majumdar, S.; Chowdhury, P. K.; Alhokbany, N.; Ahmad, T. Photoinduced hole trapping in $MoSe_2$–MoS_2 nanoflowers/ZnO nanosheets S-scheme conduit for ultrafast charge transfer during hydrogen evolution. *ACS Appl. Energy Mater.* **2024**, *7*, 2881–2895.

[12] Younas, U.; Mobeen, F.; Saleem, A.; Ali, F.; Huwayz, M. A.; Ashraf, A.; Ahmad, A.; Alwadai, N.; Pervaiz, M.; Iqbal, M. Efficient hydrogen production via overall water splitting using CuO/ZnO decorated reduced graphene oxide as bifunctional electrocatalyst. *Ceram. Int.* **2024**, *50*, 30570–30578.

[13] Zhang, B. S.; Luo, Y.; Xiang, D.; Qin, J. D.; Miao, K. H.; Wang, X.

F.; Kang, X. W.; Tian, Y. Yolk-shell structured zinc-cobalt-ruthenium alloy oxide assembled with ultra-small nanoparticles: A superior cascade catalyst toward oxygen evolution reaction. *Adv. Funct. Mater.* **2023**, *33*, 2214529.

[14] Liu, M. H.; Chen, X. X.; Li, S. Y.; Ni, C. D.; Chen, Y. W.; Su, H. Dynamic-cycling zinc sites promote ruthenium oxide for sub-ampere electrochemical water oxidation. *Nano Lett.* **2024**, *24*, 16055–16063.

[15] Zhou, Y. N.; Fan, R. Y.; Zhang, Y. S.; Yu, N.; Hu, H.; Hojamberdiev, M.; Dong, B.; Chai, Y. M. Self-catalyzed Ru redeposition based on Co, Zn-driven double anchoring for robust acidic water oxidation. *ACS Energy Lett.* **2024**, *9*, 5064–5073.

[16] Huang, Z. F.; Song, J. J.; Du, Y. H.; Xi, S. B.; Dou, S.; Nsanzimana, J. M. V.; Wang, C.; Xu, Z. J.; Wang, X. Chemical and structural origin of lattice oxygen oxidation in Co-Zn oxyhydroxide oxygen evolution electrocatalysts. *Nat. Energy* **2019**, *4*, 329–338.

[17] Huang, Y.; Wang, Z. Y.; Xiao, H.; Liu, Q. D.; Wang, X. Activating and stabilizing lattice oxygen via self-adaptive Zn-NiOOH sub-nanowires for oxygen evolution reaction. *J. Am. Chem. Soc.* **2024**, *146*, 29006–29016.

[18] Mei, Y. J.; Chen, J. L.; Wang, Q.; Guo, Y. Q.; Liu, H. W.; Shi, W. H.; Lin, C.; Yuan, Y. F.; Wang, Y. H.; Xia, B. Y. et al. MoZn-based high entropy alloy catalysts enabled dual activation and stabilization in alkaline oxygen evolution. *Sci. Adv.* **2024**, *10*, eadq6758.

[19] Liu, L.; Wang, S. Z.; Liu, W.; Wang, J. L.; Zhang, B. Q.; Yang, J. Q.; Liu, H.; Li, Y. H. Supercritical hydrothermal synthesis of nano-ZnO: Effects of key parameters and reaction mechanism. *Ceram. Int.* **2023**, *49*, 31313–31324.

[20] Bu, D. G.; Batmunkh, M.; Zhang, Y.; Li, Y. W.; Qian, B. Z.; Lan, Y. L.; Hou, X.; Li, S.; Jia, B. H.; Song, X. M. et al. Rechargeable sunlight-promoted Zn-air battery constructed by bifunctional oxygen photoelectrodes: Energy-band switching between ZnO/Cu_2O and ZnO/CuO in charge-discharge cycles. *Chem. Eng. J.* **2022**, *433*, 133559.

[21] Zhang, Y. L.; Liu, B.; Dai, Y. K.; Shen, L. X.; Guo, P.; Xia, Y. F.; Zhang, Z. Y.; Kong, F. T.; Zhao, L.; Wang, Z. B. Engineering Co-N-Cr cross-interfacial electron bridges to break activity-stability trade-off for superdurable bifunctional single atom oxygen electrocatalysts. *Angew. Chem., Int. Ed.* **2024**, *63*, e202400577.

[22] Chen, Z. B.; Huang, K.; Zhang, B. W.; Xia, J. Y.; Wu, J. S.; Zhang, Z. Q.; Huang, Y. Z. Corrosion engineering on AlCoCrFeNi high-entropy alloys toward highly efficient electrocatalysts for the oxygen evolution of alkaline seawater. *Int. J. Miner. Metall. Mater.* **2023**, *30*, 1922–1932.

[23] Kresse, G.; Hafner, J. *Ab initio* molecular dynamics for liquid metals. *Phys. Rev. B* **1993**, *47*, 558–561.

[24] Kresse, G.; Furthmüller, J. Efficiency of *ab-initio* total energy calculations for metals and semiconductors using a plane-wave basis set. *Comput. Mater. Sci.* **1996**, *6*, 15–50.

[25] Perdew, J. P.; Burke, K.; Ernzerhof, M. Generalized gradient approximation made simple. *Phys. Rev. Lett.* **1996**, *77*, 3865–3868.

[26] Kresse, G.; Joubert, D. From ultrasoft pseudopotentials to the projector augmented-wave method. *Phys. Rev. B* **1999**, *59*, 1758–1775.

[27] Blöchl, P. E. Projector augmented-wave method. *Phys. Rev. B* **1994**, *50*, 17953–17979.

[28] Bai, S. Z.; Dai, W. J.; Yang, X. Y.; Wu, B.; Guo, J.; Zhao, C. J.; Zhang, Y. D.; Cui, C.; Zou, G. D.; Huang, S. F. Phosphate-decorated hierarchical porous CoNiFe medium-entropy alloy: An efficient and low-cost electrocatalyst for seawater oxidation. *Int. J. Hydrogen Energy* **2024**, *84*, 615–622.

[29] Dai, W. J.; Yang, X. Y.; Hu, F. Y.; Cao, W. W.; Zhao, C. J.; Zhang, Y. D.; Huang, S. F. Solution combustion synthesis of hierarchical porous $CoNiFeCu_{0.1}$ medium-entropy alloy: A highly efficient and robust electrocatalyst for water oxidation. *J. Alloys Compd.* **2023**, *952*, 169987.

[30] Zhu, J. W.; Zhao, J. W.; Luan, D. Y.; Lou, X. W. Oxygen-coordinated single-atom nickel catalysts derived from water-induced metal-organic framework aerogel for efficient water oxidation. *Angew. Chem., Int. Ed.* **2025**, *64*, e202500261.

[31] Miao, F.; Jing, Z. Y.; Zhang, Z. B.; Chong, X. Y.; Liang, X. B. A self-supported 3D porous high entropy alloy with progressive formation of needle-shaped nanowires during reactions for maintained excellent electrocatalytic oxygen evolution. *Int. J. Hydrogen Energy* **2024**, *51*, 301–313.

[32] Liu, W.; Ding, X. Q.; Cheng, J. J.; Jing, J. L.; Li, T. S.; Huang, X.; Xie, P. P.; Lin, X. C.; Ding, H. L.; Kuang, Y. et al. Inhibiting dissolution of active sites in 80 °C alkaline water electrolysis by oxyanion engineering. *Angew. Chem., Int. Ed.* **2024**, *63*, e202406082.

[33] Wang, S.; Yan, Y.; Du, Y. P.; Zhao, Y. G.; Li, T. X.; Wang, D.; Schaaf, P.; Wang, X. Y. Inhibiting the deep reconstruction of Ni-based interface by coordination of chalcogen anions for efficient and stable glycerol electrooxidation. *Adv. Funct. Mater.* **2024**, *34*, 2404290.

[34] Zhong, H. Y.; Zhang, Q.; Yu, J. C.; Zhang, X.; Wu, C.; Ma, Y. F.; An, H.; Wang, H.; Zhang, J.; Wang, X. et al. Fundamental understanding of structural reconstruction behaviors in oxygen evolution reaction electrocatalysts. *Adv. Energy Mater.* **2023**, *13*, 2301391.

[35] Wang, X. H.; Zhang, Z. N.; Wang, Z.; Ding, Y.; Zhai, Q. G.; Jiang, Y. C.; Li, S. N.; Chen, Y. Ultra-thin $CoNi_{0.2}P$ nanosheets for plastics and biomass participated hybrid water electrolysis. *Chem. Eng. J.* **2023**, *465*, 142938.

[36] Li, P.; Wan, X. H.; Su, J. H.; Liu, W.; Guo, Y. Z.; Yin, H. Y.; Wang, D. H. A single-phase FeCoNiMnMo high-entropy alloy oxygen evolution anode working in alkaline solution for over 1000 H. *ACS Catal.* **2022**, *12*, 11667–11674.

[37] Zhu, J. L.; Qian, J. M.; Peng, X. B.; Xia, B. R.; Gao, D. Q. Etching-induced surface reconstruction of $NiMoO_4$ for oxygen evolution reaction. *Nano-Micro Lett.* **2023**, *15*, 30.

[38] Miao, F.; Cui, P.; Gu, T.; Sun, B.; Yan, Z. J. Engineering electronic structures and oxygen vacancies of manganese-doped nickel molybdate porous nanosheets for efficient oxygen evolution reaction. *J. Colloid Interface Sci.* **2024**, *676*, 680–690.

[39] Zhang, Y.; Chen, B. Y.; Qiao, Y. X.; Duan, Y. R.; Qi, X. Y.; He, S. Q.; Zhou, H.; Chen, J. K.; Yuan, A. H.; Zheng, S. L. FeNi alloys incorporated N-doped carbon nanotubes as efficient bifunctional electrocatalyst with phase-dependent activity for oxygen and hydrogen evolution reactions. *J. Mater. Sci. Technol.* **2024**, *201*, 157–165.

[40] Liu, H. Q.; Miao, J. H.; Wang, Y. B.; Chen, S. Y.; Tang, Y. J.; Zhu, D. D. Heterostructured $ZnFe_2O_4$@Ni_3S_2 nanosheet arrays on Ni foam as an efficient oxygen evolution catalyst. *Chem. Commun.* **2024**, *60*, 4443–4446.

[41] Miao, J.; Hong, Q. L.; Liang, L. P.; Li, G. M.; Liu, Z. H.; Yin, S. B.; Chen, Y. B and Fe Co-doped Co_2P hollow nanocubes for nitrate electroreduction to ammonia. *Chin. Chem. Lett.* **2024**, *35*, 108935.

[42] Song, R. T.; Ma, Y. Y.; Shi, M. Y.; Li, Z. F.; Liu, W. T.; Ma, W. B.; Zuo, C. L.; Zhang, H.; Nan, Z.; Sun, Y. H. Urchin-like medium-entropy oxyhydroxide FeCoNiOOH nanoparticles supported on nickel foam for seawater oxidation. *ACS Appl. Nano Mater.* **2025**, *8*, 9555–9564.

[43] Wu, B.; Dai, W. J.; Yang, X. Y.; Zhao, C. J.; Zhang, Y. D.; Cui, C.; Sui, Y.; Cao, P.; Huang, S. F. Surface reconstruction and entropy engineering of $Ni(OH)_2$ nanosheets for enhanced electrocatalytic performances of oxygen evolution reaction in alkaline seawater. *Fuel* **2024**, *374*, 132450.

[44] Pradhan, A. K.; Halder, S.; Chakraborty, C. Pt-nanoparticles on ZnO/carbon quantum dots: A trifunctional nanocomposite with superior electrocatalytic activity boosting direct methanol fuel cells and zinc-air batteries. *J. Mater. Chem. A* **2025**, *13*, 243–256.

[45] Zhi, L. H.; Zhang, M. M.; Tu, J. B.; Li, M. Phosphorus vacancies regulation and heterogeneous interfacial engineering of coral-like ZnO/FeCoPv@*N*-doped carbon hierarchical microspheres to boost overall water splitting. *J. Colloid Interface Sci.* **2025**, *678*, 1001–1011.
[46] Tian, T.; Gao, H.; Zhou, X. C.; Zheng, L. R.; Wu, J. F.; Li, K.; Ding, Y. Study of the active sites in porous nickel oxide nanosheets by manganese modulation for enhanced oxygen evolution catalysis. *ACS Energy Lett.* **2018**, *3*, 2150–2158.
[47] Feng, R. H.; Ye, Z. H.; Jiang, Q.; Li, C. W.; Gu, J. F.; Song, F. Phosphorus-doping promotes the electrochemical etching of metals to nanoporous electrodes for efficient and durable overall water splitting. *J. Power Sources* **2022**, *542*, 231774.
[48] Zhu, S. R.; Wang, X.; Le, J. B.; An, N.; Li, J. M.; Liu, D. Y.; Kuang, Y. B. Striking stabilization effect of spinel cobalt oxide oxygen evolution electrocatalysts in neutral PH by dual-sites iron incorporation. *Energy Environ. Mater.* **2024**, *7*, e12594.
[49] Ding, S.; Xia, B. K.; Li, M.; Lou, F. Q.; Cheng, C.; Gao, T. Q.; Zhang, Y. X.; Yang, K.; Jiang, L. L.; Nie, Z. H. et al. An abnormal size effect enables ampere-level O_2 electroreduction to hydrogen peroxide in neutral electrolytes. *Energy Environ. Sci.* **2023**, *16*, 3363–3372.
[50] Li, Y.; Wu, Y. Y.; Hao, H. R.; Yuan, M. K.; Lv, Z.; Xu, L. L.; Wei, B. *In situ* unraveling surface reconstruction of Ni_5P_4@FeP nanosheet array for superior alkaline oxygen evolution reaction. *Appl. Catal. B: Environ.* **2022**, *305*, 121033.
[51] Rodrigues, A. V.; Onishi, B. S. D.; Ribeiro, S. J. L. Facile formation of sulfurized nanorod-like ZnO/$Zn(OH)_2$ and hierarchical flower-like γ-$Zn(OH)_2$/ϵ-$Zn(OH)_2$ from a green synthesis and application as luminescent solar concentrator. *ChemPhysChem* **2023**, *24*, e202300134.
[52] Zhang, D. F.; Li, M. N.; Yong, X.; Song, H. Q.; Waterhouse, G. I. N.; Yi, Y. F.; Xue, B. J.; Zhang, D. L.; Liu, B. Z.; Lu, S. Y. Construction of Zn-doped RuO_2 nanowires for efficient and stable water oxidation in acidic media. *Nat. Commun.* **2023**, *14*, 2517.
[53] Ling, C. Y.; Shi, L.; Ouyang, Y. X.; Zeng, X. C.; Wang, J. L. Nanosheet supported single-metal atom bifunctional catalyst for overall water splitting. *Nano Lett.* **2017**, *17*, 5133–5139.
[54] Zheng, Y.; Jiao, Y.; Zhu, Y. H.; Cai, Q. R.; Vasileff, A.; Li, L. H.; Han, Y.; Chen, Y.; Qiao, S. Z. Molecule-level g-C_3N_4 coordinated transition metals as a new class of electrocatalysts for oxygen electrode reactions. *J. Am. Chem. Soc.* **2017**, *139*, 3336–3339.
[55] Liu, H. J.; He, Q.; Jiang, H. L.; Lin, Y. X.; Zhang, Y. K.; Habib, M.; Chen, S. M.; Song, L. Electronic structure reconfiguration toward pyrite NiS_2 via engineered heteroatom defect boosting overall water splitting. *ACS Nano* **2017**, *11*, 11574–11583.